SLaMA-URM method for the seismic vulnerability assessment of UnReinforced Masonry structures: Formulation and validation for a substructure

Article *in* Journal of Building Engineering · January 2023

DOI: 10.1016/j.jobe.2022.105487

https://doi.org/10.1016/j.jobe.2022.105487

SLaMA-URM method for the seismic vulnerability assessment of UnReinforced Masonry structures: formulation and validation for a substructure

Claudia Sansoni[1], Luís C. M. da Silva[2*], Rui Marques[3], Stefano Pampanin[4], Paulo B. Lourenço[5]

[1]Department of Structural and Geotechnical Engineering, University of Rome Sapienza, Via Eudossiana 18, 00184 Rome, Italy. e-mail: claudia.sansoni@uniroma1.it

[2]Department of Architecture, Built Environment and Construction Engineering, Politecnico di Milano, Piazza Leonardo da Vinci 32, 20133 Milano, Italy. E-mail: luiscarlos.martinsdasilva@polimi.it

[3]ISISE, Department of Civil Engineering, University of Minho, Campus de Azurém, 4800-058 Guimarães, Portugal. e-mail: marquesmnc@sapo.pt

[4]Department of Structural and Geotechnical Engineering, University of Rome Sapienza, Via Eudossiana 18, 00184 Rome, Italy. e-mail: stefano.pampanin@uniroma1.it

[5]ISISE, Department of Civil Engineering, University of Minho, Campus de Azurém, 4800-058 Guimarães, Portugal. e-mail: pbl@civil.uminho.pt

[*] Corresponding author

ABSTRACT

An analytical procedure based on the SLaMA (Simplified Lateral Mechanism Analysis) method is proposed for the seismic vulnerability assessment of UnReinforced Masonry (URM) structures. The procedure considers an equivalent frame discretization for the structure (pier, spandrel, and joint elements) and includes: (i) the evaluation of moment–rotation capacity curves at each pier-spandrel subassembly; (ii) the assessment of the hierarchy of strength in each subassembly; and (iii) the calculation of the structure capacity curve according to the expected failure mechanism. Validation of the proposed SLaMA-URM procedure is achieved in a one-story URM substructure tested under lateral cyclic loading. The analytical predictions are compared with numerical ones from a 2D continuous finite element (FE) model based on a macro-modelling strategy. The flexural capacity of the components is estimated using a monolithic beam analogy, and the results compared with those from traditional sectional analysis. The influence of the substructure geometry on the hierarchy of strength at the subassembly and global levels is investigated. An analytical formulation of the pier-spandrel joint strength is also proposed to be considered in the assessment of the hierarchy of strength. The method is validated for a one-story substructure subjected to lateral in-plane loading. Results, in terms of crack patterns and capacity curves, are in relatively good agreement with the experimental and FE results, even when a bilinear curve approximation is used. The potential of the SLaMA-URM method for the seismic assessment of URM buildings is thus demonstrated, whose application to a larger URM structure is planned as a subsequent study.

Keywords: URM structures, lateral mechanism analysis, pier-spandrel joint, simple benchmark substructure, numerical simulation, geometry influence.

1. Introduction

Past and recent earthquakes, such as the 2016 Central Italy earthquakes, evidenced the high seismic vulnerability of UnReinforced Masonry (URM) buildings. To deal with this problem, it is necessary at first to understand the actual behavior of masonry structures, identify their critical weaknesses (diagnosis), assess their seismic vulnerability (prognosis), and implement effective prevention strategies (therapy).

Masonry is a composite material, for which advanced modeling approaches based on the Finite Element (FE) method have been developed to simulate its complex behavior [1–7]. Although this strategy can potentially provide very accurate results, it is computationally demanding and, therefore, of limited application in seismic vulnerability assessment studies. Simplified models are usually preferred, since they allow a good compromise between the computational burden and the reliability of the results, e.g. [8–15]. Within this context, the Equivalent Frame (EF) method is arguably the most frequently used. When applying the EF method to URM structures, the influence of the pier-spandrel joint (considered rigid) is generally neglected, both in terms of strength and deformability, as originally proposed by Dolce [16].

In this work, a simplified mechanical-based analytical ("by-hand") procedure, based on the EF discretization, is proposed for the seismic vulnerability assessment of URM structures. This procedure builds on and extends the SLaMA (Simplified Lateral Mechanism Analysis) method in the New Zealand Seismic Assessment guidelines (NZSEE Part C5 [17]) and recent Dutch guidelines NPR 9998-18 [18]. The SLaMA method is based on an analytical nonlinear approach to obtain the capacity curve of a given frame-like Reinforced Concrete (RC) structure through simple hand calculations [19,20] and, more recently, to masonry structures [21].

The global seismic response of the structure is integrated from the components capacity by considering a "chain" of failure mechanisms among the structural subassemblies. The sequence of mechanisms relies on the hierarchy of strength between the structural components using a

Moment–Axial load (M–N) performance domain [22]. The equilibrium approach is based on the distribution of the internal "moment capacity" at each subassembly, to derive the equivalent frame Overturning Moment (OTM) and, in turn, the base shear versus lateral displacement capacity curve.

The so-called SLaMA-URM method proposed here is intended to be a tool to quickly assess the seismic capacity of URM structures. The presented application of the method is intended to give a comprehensive overview of the methodology. The subsequent parametric analyses are aimed to address the influence of the pier-spandrel joint, as well as of the dimensions of the panels, on the global response of a simple URM structure.

2. Proposed SLaMA-URM method

The SLaMA method is currently prescribed in several guidelines (the NZSEE Part C5 [17] and the NPR 9998-18 [18]) for the seismic assessment of existing buildings, as a key stage in the procedure before the implementation of more complex computational models. The methodology consists of several consequential steps: 1) obtaining the building data (geometry, material properties and details) and the information on the seismic hazard; 2) evaluating the flexural and shear capacities at the component level; 3) defining the hierarchy of strength among column, beam and joint at subassembly level; 4) evaluating the overturning moment capacity of the structure and the overall force–displacement response (corresponding to either column-sway, beam-sway or mixed sideways mechanisms) from the equilibrium of the internal moment capacities.

In this work, the SLaMA method is extended, adapted, and applied to the case of URM structures, relying on the hypothesis of regular and frame-like buildings. The capacity of structural components, such as the in-plane flexural and shear strengths, are defined according to rules given in the literature and/or code provisions. The proposed method relies on the hypothesis of building box-behavior, so the influence of the out-of-plane response of the walls and the deformability of the floors is disregarded. This is currently a limitation of the method, but its application to geometrically regular buildings according to the assumption of box-behavior, i.e., with good wall-to-wall and wall-to-floor connections and stiff diaphragms is reasonable. In this case, the response of the building in each direction can be calculated as the sum of the responses of the individual walls oriented in that direction. Further improvements to the method aiming to consider both the out-of-plane response of the walls and the deformability of the floors will be considered in a next step, in which experimental works that may constitute a valuable source of validation can be found in [23,24].

2.1 Background of considered strength criteria

Several models for estimating the in-plane strength of URM piers are available in the literature. The flexural strength related to the rocking mechanism is typically defined assuming an equivalent rectangular compressive stress block (NTC 2018 [25], NZSEE Part C8 [26]). For the shear strength, several formulations exist to consider the different mechanisms of diagonal cracking and bed-joint sliding. For diagonal cracking, the Turnšek and Cačovic [27] criterion, in which the strength is defined based on the masonry tensile strength, and the Mann and Müller [28] model, that assumes the shear strength based on the cohesion and the friction coefficient of joints, are the two most common approaches in masonry codes. For bed-joint sliding, the Mohr-Coulomb criterion is typically assumed, as suggested in the Italian code (NTC 2018 [25]). For URM spandrels, there is a limited knowledge on their behavior and the experimental studies are scarce and relatively recent (e.g., Beyer and Dazio [29], Parisi et al. [30], Knox et al. [31]). According to some building codes, if a spandrel is coupled by an effective lintel or by tie-rods, it can be assumed as a pier rotated by 90 degrees (e.g., NTC 2018 [25], EN 1998-3 [32]). This is specifically addressed in NTC 2018 [25], when the horizontal axial load is known; otherwise, an equivalent strut is assumed (if a coupled tensile resistant element is present) and the shear strength depends on the cohesion. In absence of any specific resistant element coupled to the spandrel, the bricks interlocking effect at the end-sections with the contiguous masonry can be considered (FEMA 306 [33], Cattari and Lagomarsino [34]) to avoid an excessive underestimation of the flexural capacity.

In the EF modeling approach, the evidence of limited damage to pier-spandrel joints in URM walls during earthquakes has led to assume them as rigid and infinitely resistant. However, joints may have an important role on both buildings' stiffness and capacity depending on the geometry of the spandrel-pier subassemblies. This has been observed experimentally in [29,31,35], but also in recent numerical studies [36–38]. The assumption of deformable joints may better capture the real behavior of buildings, especially because a rigid node assumption is a rough approximation of the complex stress transfer mechanism that occurs between spandrels and piers, as addressed by [39]. In such a context, the actual capacity of the joints can be considered by assuming an "equivalent strut" strength mechanism (Bertoldi et al. [40]). For the EF approach, different studies have been developed to define the effective deformable height and length of piers and spandrels, respectively (e.g., Dolce [16], Lagomarsino et al. [41]).

In the SLaMA method, a specific sectional analysis procedure is implemented according to the Monolithic Beam Analogy (MBA) approach aiming to estimate the moment–rotation capacity of components. This approach is based on the calculation of the equilibrium of deformable bodies, as in the case of precast concrete jointed ductile rocking-dissipative connections based on unbonded post-tensioned techniques (Pampanin et al. [42]).

2.2 Component level analysis: piers and spandrels

2.2.1 *Moment–Rotation curves*

The flexural capacity of piers is defined from an elastic–perfectly plastic stress–strain relation in compression and no-tensile resistance (EPP-NTR) assumption. Regarding the spandrels, an elastic–perfectly plastic stress-strain in compression and tension resistant (EPP-TR) model is considered. In detail, an equivalent tensile strength f_{tu} related to the interlocking effect [34] is used to calculate the bending moment by performing the sectional analysis. Based on the height and the width of the bricks, Δ_y and Δ_x, respectively, and considering the 65% of the mean compressive vertical stress σ_v on the cross-section of the adjacent pier, the equivalent tensile strength is calculated according to Equation (1) [34].

$$f_{tu} = \frac{\Delta_x}{2\Delta_y} \mu \, 0.65 \, \sigma_v \tag{1}$$

where μ is the friction angle. The stress–strain relationships in compression and tension used in the sectional analysis for describing the moment–rotation response, with the corresponding elastic (ε_{yc} and ε_{yt}) and ultimate (ε_{uc} and ε_{ut}) strain values, are shown in Figure 1.

Note that the responses are defined at an element scale, rather than at a representative volume of the masonry. At an element scale, there is some evidence that the consideration of an EPP model with significant ductility in tension is a reasonable assumption for spandrels, e.g., Cattari and Lagomarsino [34]. Note that the tension resisting response is considered only for the spandrel (Figure 1b). In fact, when the damage of spandrels is mostly driven by shear cracking of the mortar bed joints, as assumed in the current work, the failure is relatively ductile. A brittle failure is more likely to occur due to the tensile cracking of the units and so in a weak-unit–strong-joint masonry, as observed in [3].

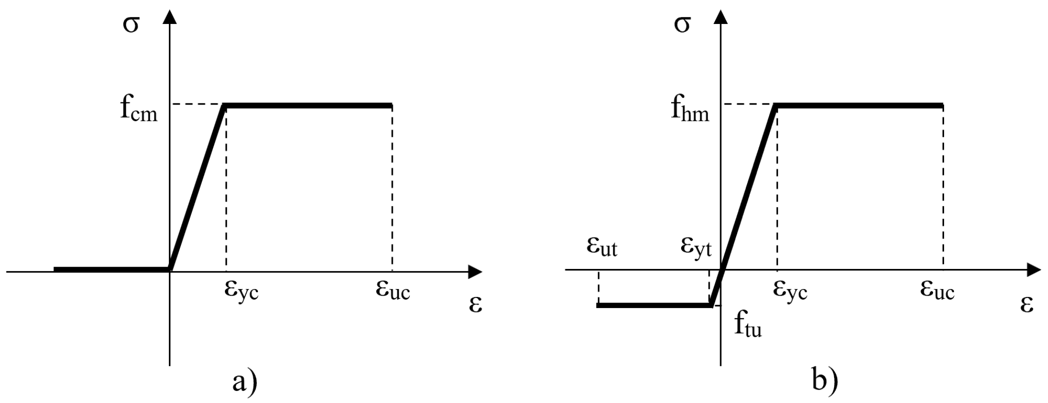

Figure 1. Stress-strain relationships: (a) elastic–perfectly plastic in compression and no-tensile resistant (EPP-NTR) for piers, and (b) elastic–perfectly plastic in compression and tensile resistant (EPP-TR) for spandrel.

The MBA formulation (Pampanin et al. [42]) is herein adapted for URM structures to characterize the step-by-step rocking/rotation behavior of piers and spandrels. In particular, the components are assumed as deformable bodies with the inelastic deformations concentrated at their ends, whose position is established by the existing openings. Therefore, Equation (2) can be derived from an analogy in terms of displacement (member compatibility condition) between the URM cantilever element and an equivalent monolithic RC element.

$$\theta_i = \frac{\left(\frac{\varepsilon_i}{c_i} - \chi_y\right)\left(L_{cant} - \frac{L_p}{2}\right)L_p}{L_{cant}} \tag{2}$$

where ε_i is the strain value at the corresponding neutral axis depth c_i, $\chi_y = 2\,\varepsilon_{yc}/B$ is the elastic curvature (where B is taken as the length B_p for piers and the height h_{sp} for spandrels), L_{cant} is the distance from the element-end to the point of contraflexure (assumed as half of the effective height for piers, $h_{p,eff}/2$, and as half of the clear span for spandrels, $L_{sp}/2$), and L_p is the assumed cracking depth (theoretical equivalent plastic hinge length) at the element-end, which is taken approximately as $0.1L_{cant}$. This last estimation of L_p according to [42] can be adopted in cases with a limited knowledge about the masonry arrangement. For well-known cases, based on damage evidence in experimental programs for piers and spandrels [29,43,44], L_p can be estimated according to the masonry units dimensions. Specifically, assuming L_p ranging between $[h_{unit}, 2h_{unit}]$ and $[\ell_{unit}, 2\ell_{unit}]$ for piers and spandrels, respectively, is a good compromise; where ℓ_{unit} is the length of units and h_{unit} is the height of units. Considering that Equation (2) defines only the "plastic" component of the element's rotation, developed through the rocking mechanism, the elastic component (flexural and shear deformations of the member itself outside the critical rocking sections) is added from the initial stiffness K_{el} according to Equation (3), after assuming fixed-fixed boundary conditions.

$$K_{el} = \left(\frac{{h_{eff}}^3}{12E_m I} + 1.2\frac{h_{eff}}{B_p t_p G_m}\right)^{-1} \tag{3}$$

where h_{eff} is the effective height (derived from Dolce's [16] rule for piers, $h_{p,eff}$, and given by the clear span for spandrels, L_{sp}), B_p and t_p are respectively the length and the thickness of the element, E_m and G_m are respectively the elastic and shear moduli of masonry, and I is the moment of inertia. For spandrels, the moment capacity curve is defined in two different ways according to the EPP-TR model, which are characterized by: 1) ductility in tension limited to $\mu_{\varepsilon t} = \varepsilon_{ut}/\varepsilon_{yt} = 50$, i.e., tension-governed failure (TF), and 2) ductility in compression limited to $\mu_{\varepsilon c} = \varepsilon_{uc}/\varepsilon_{yc} = 1.2$ with infinite ductility in tension, i.e., compression-governed failure (CF). The tension strain ductility of $\mu_{\varepsilon t} = 50$ was calculated according to the generalized EPP tension stress–strain model for spandrels (i.e., $\varepsilon_{yt} = 0.04\%$ and $\varepsilon_{ut} = 2\%$) defined by Knox [42], when considering that damage is mostly driven by the shear cracking of the mortar bed joints. The Knox's proposal [42] is based on results from in-situ bed-joint shear tests in typical New Zealand masonry buildings.

Three different limit state conditions are considered (decompression, peak and ultimate) and a sectional analysis is performed to define the moment–rotation response. In detail, the decompression condition corresponds to the assumption that the rotation θ_{dec} is equal to the elastic rotation (obtained from the initial stiffness K_{el}), and the decompression moment M_{dec} is consequently defined. For piers and spandrels, when the EPP-TR-CF model is adopted, from imposing the values of compressive peak ε_{yc} and ultimate ε_{uc} strains, the peak moment M_p and the ultimate moment M_u, and the corresponding rotations (elastic plus plastic) θ_p and θ_u, are defined. On the contrary, when the EPP-TR-TF model is adopted for spandrels, from imposing the values of tensile peak ε_{yt} and ultimate ε_{ut} strains, the moments M_p and M_u and the corresponding rotations θ_p and θ_u, are defined.

Regarding the shear strength of piers, the Turnšek and Cačovic [27] criterion is adopted for diagonal cracking, given by Equation (4).

$$V_{s,dc} = \frac{B_p t_p f_t}{b}\sqrt{1+\frac{\sigma_v}{f_t}} \tag{4}$$

in which $b = h_{p,eff}/B_p$ is the pier aspect ratio that varies in the range [1–1.5], f_t is the masonry tensile strength, and σ_v is the compressive vertical stress on the pier. The Mohr-Coulomb criterion is assumed for bed-joint sliding, as given by Equation (5).

$$V_{s,bdj} = l' t_p (f_{v0} + \mu\sigma_v) \tag{5}$$

where l' is the compressed length of the pier, f_{v0} is the masonry shear strength in absence of axial load, and μ is the masonry friction coefficient (assumed to be $\mu = 0.7$). It is noteworthy to highlight that Equation (5) is an implicit expression, since the l' value is dependent on the lateral shear force. Several authors tried to overcome this dual dependence, for instance [45]. For spandrels, the shear strength is calculated with Equation (6), multiplying the spandrel cross-section (height h_{sp} × thickness t_p) by the masonry shear strength in absence of axial load, f_{v0} (NTC 2018 [25]).

$$V_{s,dc} = h_{sp} t_p f_{v0} \tag{6}$$

The strength thresholds are expressed in terms of moment capacity calculated from the pier (or spandrel) shear resistance V_s and the pier (or spandrel) cantilever length L_{cant}, as $M = V_s L_{cant}$.

2.2.2 *Moment–Axial load (M–N) performance domains*

The flexural capacity of piers is defined through a closed-form equation according to NTC 2018 [25] and NZSEE Part C8 [26] codes, in which the bending moment capacity is defined based on assuming an equivalent compressive stress block. Alternatively, the Moment–Axial load (*M–N*) interaction curve can be obtained through sectional equilibrium equations, in which different constitutive laws can be adopted for masonry. In such a context, the pier *M–N* interaction domains are defined by considering an elastic–perfectly plastic law in compression and a no-tensile resistant (EPP-NTR) model. The MBA approach [42] can be used for calculating the flexural capacity as an alternative to the traditional sectional analysis. It is schematized for piers in the flowchart of Figure 2.

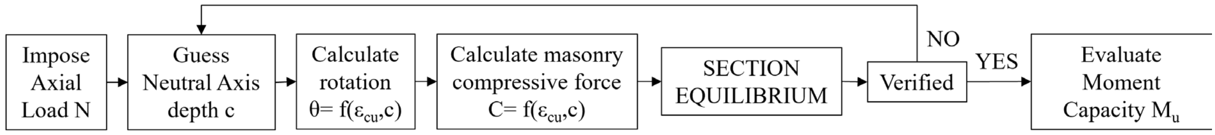

Figure 2. Calculation of the *M–N* domain through sectional analysis using the MBA approach.

2.3 Subassembly level analysis: hierarchy of strength

The evaluation of the hierarchy of strength between the structural components of a subassembly requires the assessment of the individual capacities of the components with reference to a common parameter. In the procedure proposed here, the parameter taken is the equivalent bending moment at the involved pier, according to [22].

Considering that the capacity of the structural components was previously derived as a moment–rotation relation, the pier *M–N* interaction (or performance) domain is adopted to identify the sequence of failure mechanisms in each pier-spandrel subassembly. In this performance domain, the demand is represented by the axial load variation due to the lateral load on the frame structure. The axial load variation on the piers (ΔN), due to the coupling effect of the spandrel strip during the lateral sway, is considered and introduced in the *M–N* domain, according to Equation (7) from NZSEE Part C5 [17].

$$\Delta N = \pm \frac{2H}{3L} F \tag{7}$$

where H and L are the height and the length of the substructure, respectively, and F represents the equivalent seismic load, assumed to be applied at $2/3$ of H. The intersection of the demand (axial load variation) with the capacity curves determines the sequence of events. Such assumption of considering the axial load variation follows the strategy adopted in other literature studies [19,20,46]. This strategy to evaluate the variation of axial load with reference to a single pier in a simple framed structure is as specified in section C5.6.2 of the NZSEE Part

C5 [17] guidelines. For more complex structures, a similar procedure can be adopted based on the portal frame method, or it can be computed in FE-based structural analysis software.

2.4 Global level analysis: capacity curve

The Overturning Moment (OTM) is calculated, with reference to a single-bay single-story substructure, with Equation (8) that considers a global equilibrium approach by including two contributions: 1) the sum of bending moments at the base of each pier $M_{p,i}$ and 2) the push-pull overall moment due to the coupling of shear forces at the spandrel-end V_{sp} (rocking mechanism) which is multiplied by the total length of the frame, L.

$$OTM = \sum M_{p,i} + \left(\sum V_{sp}\right) L \tag{8}$$

The base shear force V_b, given by Equation (9), is calculated dividing the OTM by the effective height of the structure H_{eff}, given by Equation (10), as formulated in Priestley et al. [47].

$$V_b = \frac{OTM}{H_{eff}} \tag{9}$$

$$H_{eff} = \frac{\sqrt{9 - 8\beta_F} - 1}{n^{0.25}} H \tag{10}$$

where $\beta_F = \frac{M_{\Delta N}}{OTM}$ is the parameter that lets to define the moment contribution of the spandrel, defined as $M_{\Delta N} = \left(\sum V_{sp}\right)L$, to the *OTM;* and n is the number of stories. The step-by-step procedure for application of the SLaMA-URM method is summarily described as follows (more details in Appendices A and B):

Step 1: Building data: Identification of the geometry, material properties and structural details

Step 2: Component level: Definition of the flexural capacity (according to Section *Moment–Rotation curves*), and the shear strength of URM piers (Eqs. (4)-(5)) and spandrels (Eq. (6))

Step 3: Subassembly level: Establishment of the hierarchy of strength

- Define the equivalent pier moment of the URM components
- Calculate the axial load variation on the piers (Eq. (7))

- Compare the capacity of the components (i.e., equivalent pier moment) with the seismic demand (i.e., axial load variation on the piers) in the pier *M–N* performance domain

Step 4: Global structural level: Definition of the pushover curve

- Calculate the overturning moment, *OTM* (Eq. (8))
- Define the effective height of the structure (Eq. (9))
- Calculate the base shear force (Eq. (10))

The above strength criteria and formulations are the ones adopted in the application of the SLaMA-URM method proposed in this work. Note that other strength criteria and formulations can be used; for instance, according to [29,34,48].

3. Experimental test and numerical simulation for validation

The experimental shear test of a benchmark structure is presented herein together with the corresponding performed numerical simulation based on a 2D macro-mechanical model. The structure consists of a pier-spandrel assembly. The results provided here are later used for validating the SLaMA-URM method. It is important to remark that future works may include the analysis of larger structures and comparison with results retrieved from advanced numerical simulations, e.g. [49,50].

3.1 Experimental setup and results

The considered substructure is designated as PS3 and was tested under in-plane lateral quasi-static cyclic loading by Knox et al. [31], see Figure 3. This is a one-story URM framed substructure with two piers linked by a spandrel, which was selected here because of its simple geometric configuration. The PS3 specimen presents a total height of 2.74 m (with piers and spandrel heights of 1.80 m and 0.94 m, respectively) and a total length of 4.42 m (with piers and spandrel lengths of 1.19 m and 1.24 m, respectively). It is a two-wythe (230 mm thick) masonry wall built reusing clay bricks obtained from a demolished 1930s URM building, and a weak mortar with an average compressive strength of 2.9 MPa, selected to simulate weather-deteriorated mortar typical of old URM buildings.

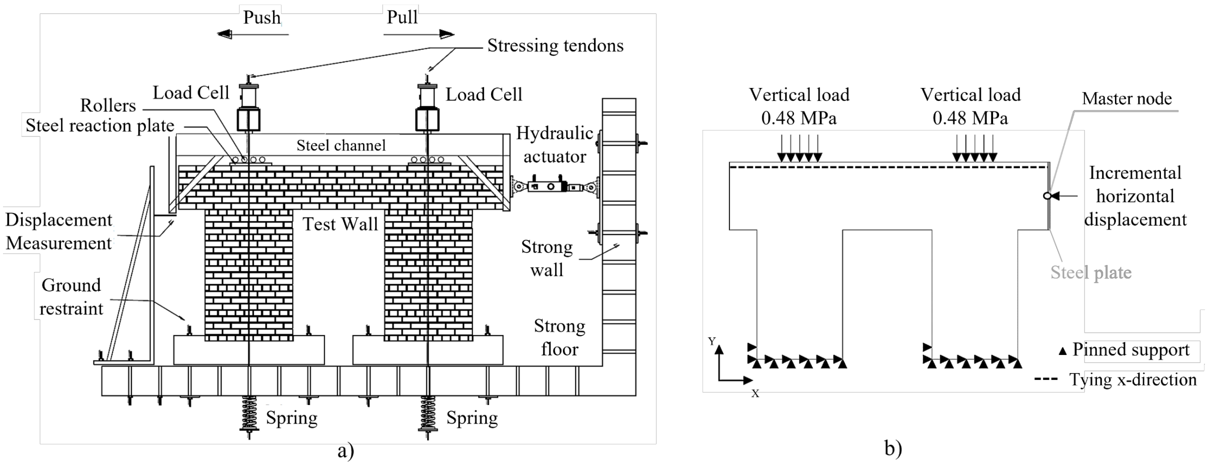

Figure 3. Benchmark tested substructure: (a) cyclic testing setup (adapted from Knox et al. [31]) and (b) sketch of the adopted boundary conditions.

The lateral load was applied on the side edges of the spandrel using a hydraulic-powered actuator connected to a reaction wall. The axial load is equal to 0.48 MPa and is equivalent to two stories of masonry. This load was applied on the top of the spandrel at the centerline of the piers. During testing, diagonal tension cracking of the spandrel characterized by a “X” crack pattern occurred before any damage in the piers. A flexural crack at the interface between the spandrel and the pier-spandrel joints was also observed earlier in the test due to the onset of the rocking mechanism [34]. The base shear–displacement response is governed by the rocking mechanism. It was reported that the test was stopped at 1% drift, without failure of the piers and so with a “ductile” flexural-rocking behavior.

3.2 Numerical simulation: 2D macro-mechanical model

This section is intended to provide a complementary view of the behavior of the tested substructure, particularly to what concerns the expected damage patterns and the sensitivity to changes in the boundary conditions and material parameters. This is particularly relevant because the latter aspects are hardly perceived from the experimental results. Furthermore, the comparison of the proposed SLaMA-URM method with a smeared-crack FE model (i.e., the

Total Strain crack model) is of relevance for practice. Such FE-based approach is widely validated in the literature and is typically adopted when studying large-scale masonry structures, e.g., Mendes and Lourenço [49] and Saloustros et al. [50].

The PS3 substructure was modeled in DIANA software [51] adopting a 2D FE macro-mechanical approach. The masonry is represented through continuum FEs (Q8MEM, 4-node quadrilateral) using a structured mesh with an approximated size of 50 mm. The Total Strain Rotating crack model was adopted to describe the material response. Regarding the coordinate system and the boundary conditions, it was considered to: (i) define the X- and Y- directions in the wall plane (Figure 4a); (ii) set the X-direction in the horizontal direction at the level of the first bottom masonry course, to simulate the concrete grouted base; (iii) adopt a master-slave node strategy, with the master node at mid-height of the right edge of the spandrel, to simulate the lateral loading by applying a horizontal displacement to the spandrel edge. A thin steel plate (10 mm thick) was modeled at the right edge of the spandrel to evenly transfer such nodal displacement to the substructure, as illustrated in Figure 3b and Figure 4a.

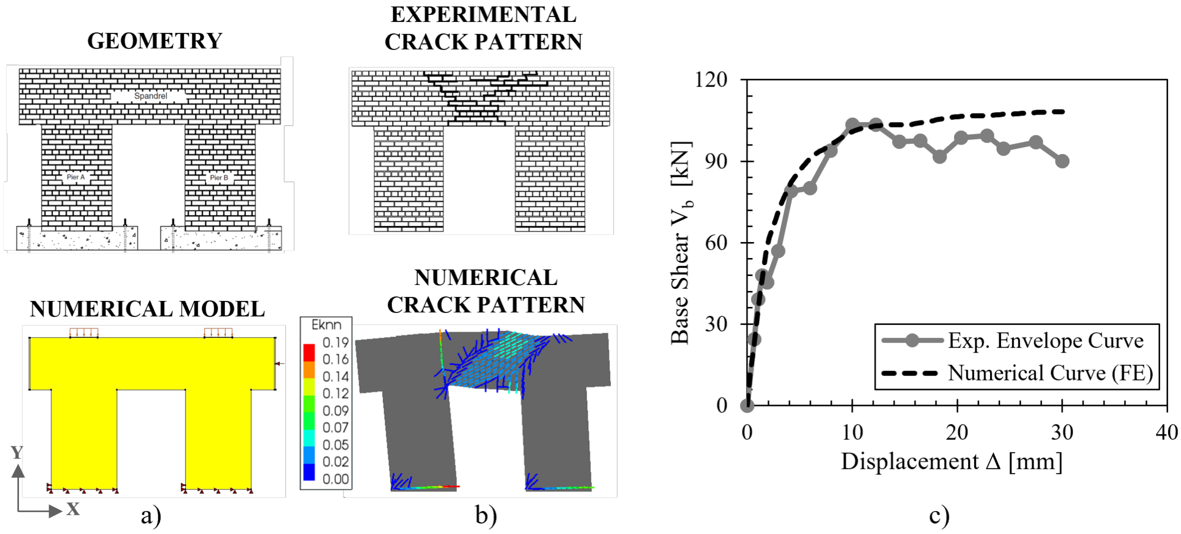

Figure 4. Simulation of the PS3 substructure: (a) geometry and FE model, (b) experimental and numerical crack patterns (normal crack strain) at the ultimate displacement and (c) numerical capacity curve against experimental envelope.

The following mechanical properties were considered in the FE model: Young's modulus $E_m = 1200$ MPa and shear modulus $G_m = 545$ MPa; for the tensile behavior, a linear-exponential stress–strain relation with strength $f_t = 0.3$ MPa and fracture energy $G_t = 0.02$ N/mm (set according to Lourenço [52], in absence of further experimental data); for the compressive behavior, a linear-parabolic stress–strain relation with strength $f_{cm} = 9.2$ MPa and fracture energy $G_c = 1$ N/mm (assumed as 1% of f_{cm}). A distributed vertical load corresponding to the axial stress on the piers of $\sigma = 0.48$ MPa was applied. The horizontal displacement was applied on the right edge of the spandrel to simulate the first push cycle experimental loading.

Pushover analysis was performed to predict the envelope of the experimental cyclic base shear–horizontal displacement response. The experimental and numerical crack patterns (in terms of normal crack strain), as well as the comparison of the corresponding base shear–displacement curves, are shown in Figure 4b-c. As observed, the numerical damage mechanisms of both piers and spandrel match well the experimental ones, i.e., rocking of piers and diagonal cracking of the spandrel. The obtained pushover curve is in good agreement with the experimental envelope response. These results are later used as a reference to assess the accuracy of the SLaMA-URM method.

It is of utmost importance to address that several assumptions follow a conservatism nature, while other are non-conservative, for example, the consideration of an elastic–perfectly plastic behavior for masonry. Although there is a certain compensation effect, one would expect that the analytical response leads to a safety solution from a practical standpoint, i.e., it is conservative. If the analytical response is directly compared with the experimental response based on a monotonic test, then it would be expected that the results of the proposed strategy would demonstrate a marked conservative nature. This was demonstrated in [53], where a monotonic loading of a given structure lead, depending on the testing protocol, to a capacity higher than that corresponding to the envelope of the cyclic lateral loading.

4. Application of the SLaMA-URM method

The SLaMA-URM procedure is herein validated with reference to the experimental case study (the so-called PS3 substructure from Knox et al. [31]) and the performed numerical simulations.

4.1 Building data: geometry and mechanical parameters

The geometry of the PS3 substructure was defined according to the EF model discretization (Figure 5) towards the application of the SLaMA-URM procedure. In detail, the length and the clear height of both piers were set to $B_p = 1.19$ m and $h_p = 1.80$ m, respectively; the height and the length of the spandrel were $h_{sp} = 0.94$ m and $L_{sp} = 1.24$ m, respectively; the thickness of both piers and spandrel was $t_p = 0.23$ m. The effective height of the piers, calculated using the Dolce's [16] rule, was $h_{p,eff} = 2.25$ m, while the effective length of the spandrel L_{sp} is its clear span.

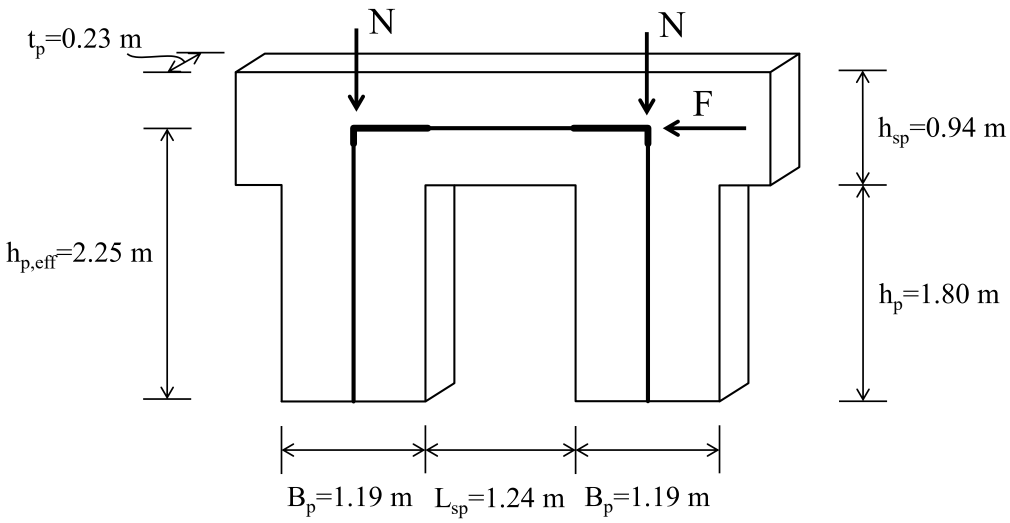

Figure 5. Schematic representation of the PS3 substructure according to the EF model.

The masonry mechanical properties adopted in the analytical model were those derived from the experimental characterization tests reported in Knox et al. [31], i.e., a masonry compressive strength f_{cm} of 9.2 MPa (the horizontal compressive strength f_{hm} was assumed equal to f_{cm} as addressed in Beyer and Dazio [29]), a brick compressive strength f_b of 25.4 MPa, and a masonry friction coefficient μ of 0.7. From the calibrated numerical model, the Young's modulus E_m and the shear modulus G_m were assumed as 1200 MPa and 545 MPa, respectively. The tensile strength f_t was calculated according to Equation (1), resulting in a value of 0.30 MPa. The shear strength at zero compressive stress f_{v0} was estimated as $f_t/1.5$ (NTC 2018 [25]), i.e., equal to 0.2 MPa. An equivalent axial load N of 131 kN, corresponding to an axial load ratio $v_r = N/(f_{cm}A_{pier}) = 0.05$ (where A_{pier} is the pier cross-section area), was applied on each pier.

4.2 Component level analysis: piers and spandrel

At the component level, the flexural and shear capacities of the piers and the spandrel are calculated, both in terms of moment–rotation curves and moment–axial load (*M*–*N*) domains. It should be noted that both PS3 substructure piers have the same geometry and pre-compression load. Moreover, their capacity and the resulting failure mechanism are dependent on the acting axial load that results from the gravity load N and the effect of axial load variation $\pm\Delta N$, due to the coupling effect of the spandrel during the lateral sway (Figure 6). The variation of the axial load ΔN is obtained from the spandrel shear resistance V_{sp} and given as the minimum of the flexural and shear strength capacities. Applying the equivalent seismic force from right to left, following the first push cycle load of the experimental test (Knox et al. [31]), the right pier is subjected to a decrease of axial load ($-\Delta N$) and the left pier to an increase of axial load ($+\Delta N$).

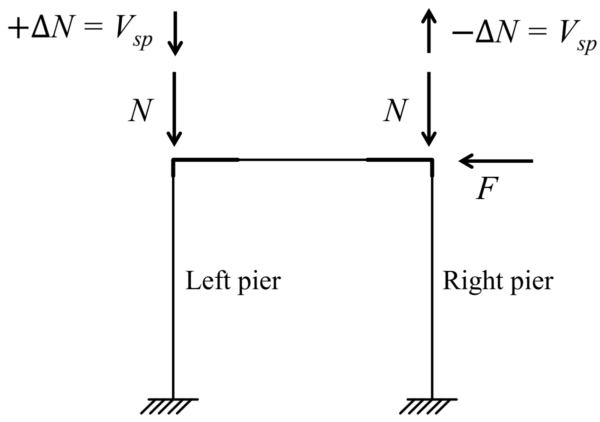

Figure 6. Frame subjected to horizontal load and gravity load with axial load variation.

The parameters adopted for the stress–strain relationships of piers (by an EPP-NTR model) and spandrel (by an EPP-TR model) are reported in Table 1. The moment–rotation couple of values obtained with the EPP-TR-CF and EPP-TR-TF models for the spandrel and those obtained with the EPP-NTR model for the piers are reported in Table 2. For the spandrel, the EPP-TR-TF model is adopted as it gives lower rotation values, hence the lower flexural ductility.

Table 1. Parameters adopted for the stress-strain relationships of piers (by an EPP-NTR model) and spandrel (by an EPP-TR model).

Structural element	**Model**	ε_{yc} **[-]**	ε_{uc} **[-]**	$f_{cm}(=f_{hm})$ **[MPa]**	ε_{yt} **[-]**	ε_{ut} **[-]**	f_{tu} **[MPa]**
PIERS	EPP-NTR (a)	0.010	0.012	9.20	-	-	-
SPANDREL	EPP-TR (b)	0.010	0.012	9.20	0.0004	0.020	0.30

Table 2. Rotation (θ) and bending moment (M) values obtained for the spandrel and piers, respectively, for the: (i) decompression instant, i.e., θ_{dec} and M_{dec}; (ii) peak instant, i.e., θ_p and M_p; (iii) and ultimate instant, i.e., θ_u and M_u.

Structural component	**Model**	θ_{dec} **[%]**	M_{dec} **[kNm]**	θ_p **[%]**	M_p **[kNm]**	θ_u **[%]**	M_u **[kNm]**
SPANDREL	EPP-TR-TF	0.149	26.28	0.187	27.08	0.290	27.08
	EPP-TR-CF	0.159	27.29	0.355	28.52	1.442	29.65
LEFT PIER	EPP-NTR	0.290	85.67	0.785	94.24	1.046	95.40
RIGHT PIER		0.156	45.90	1.272	49.98	1.782	50.28

The flexural and shear strength thresholds for the spandrel are shown in Figure 7a. It is observed that a flexural-shear mixed failure is expected to occur. Nevertheless, a brittle shear failure mechanism, which disregards the development of a flexural failure, is conservatively assumed. This results in an elastic–brittle response of the spandrel with a failure moment M_p of 26.81 kN.m. To analyze the piers, the shear strength of the spandrel V_{sp} (equal to the axial load variation ΔN on the piers) is obtained from the spandrel failure moment, as $V_{sp} = M_p\, L_{sp}/2$, resulting in $\Delta N = 43.24$ kN. Considering the gravity load N on each pier, the axial loads applied on the left and right piers are 174.6 kN and 88.1 kN, respectively. The response of both piers is governed by a rocking mechanism, as observed in Figure 7b-c. The thresholds of the flexural and shear strengths of the spandrel and the piers are reported in Table 3 and shown in Figure 7 within moment–rotation diagrams.

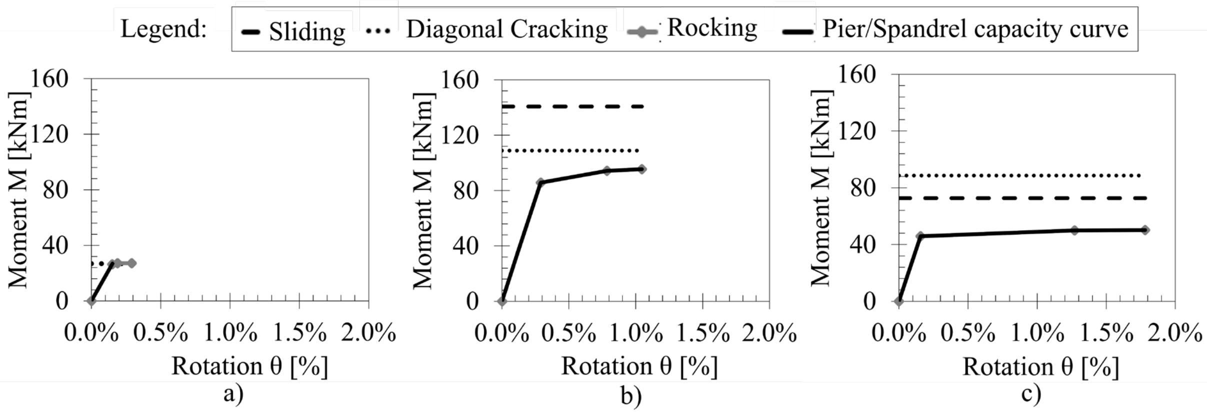

Fig. 7. Flexural and shear strength thresholds at the moment-rotation diagram for (a) spandrel (EPP-TR-TF model), (b) left pier (EPP-NTR model) and (c) right pier (EPP-NTR model).

Table 3. Rotation (θ) and bending moment (*M*) values obtained for the spandrel (EPP-TR-TF model) and piers (EPP-NTR model), respectively, for the: (i) decompression instant, i.e., θ_{dec} and M_{dec}; (ii) peak instant, i.e., θ_p and M_p; (iii) and ultimate instant, i.e., θ_u and M_u.

Structural element	θ_{dec} [%]	M_{dec} [kNm]	θ_p [%]	M_p [kNm]	θ_u [%]	M_u [kNm]	Failure
SPANDREL	0.149	26.28	0.152	26.81	0.152	26.81	*SHEAR*
LEFT PIER	0.290	85.67	0.785	94.24	1.046	95.40	*ROCKING*
RIGHT PIER	0.156	45.90	1.272	49.98	1.782	50.28	*ROCKING*

By considering a fixed elastic compressive strain $\varepsilon_{yc} = 1\%$, two different ductility levels in compression ($\mu_{\varepsilon c}$ equal to 1.2 and 3.5) are considered to evaluate the influence of the ductility on the *M–N* strength domain for piers. It is noteworthy to state that the ε_{yc} value was assumed based on the data by Lumantarna et. al [54], from extensive masonry compression tests of laboratory constructed prisms using historical bricks, and field samples collected from heritage buildings damaged after the Christchurch earthquake of February 2011.

The results presented in Figure 8 denote that the domains from EPP-NTR model with $\mu_{\varepsilon c}$ equal to 1.2, obtained from the conventional sectional analysis and the MBA approach, converge to those based on NTC 2018 [25] or NZSEE Part C8 [26]. When increasing the ductility to a value of $\mu_{\varepsilon c} = 3.5$, the *M–N* domain expands since the neutral axis depth decreases and, consequently, the lever arm of the resultant compression force increases. In all cases, the *M–N* curves obtained with the two approaches, i.e., the conventional sectional analysis and the MBA approach, show a perfect agreement.

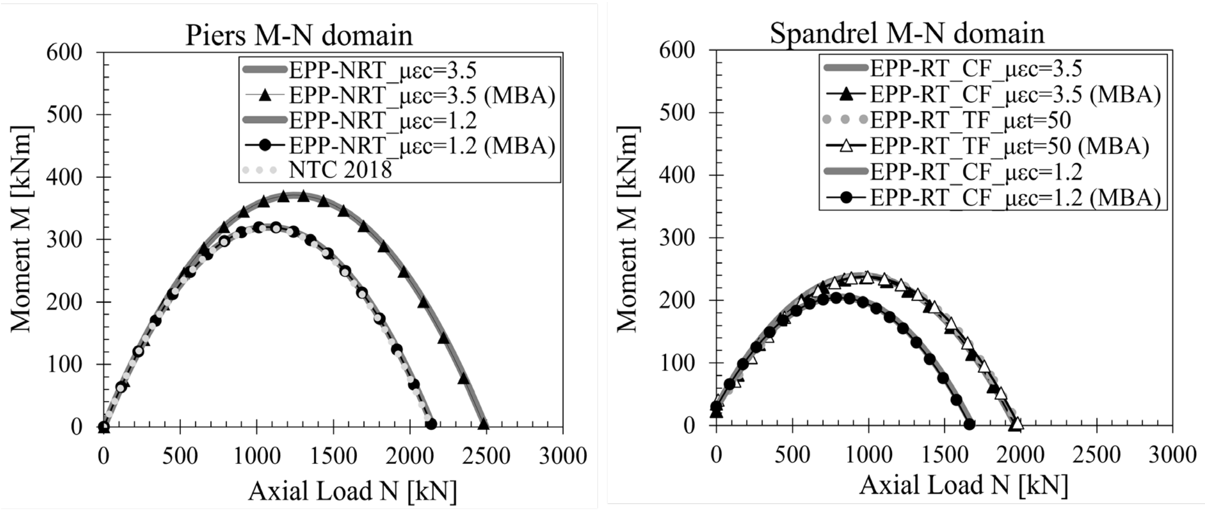

a) b)

Figure 8. Comparison of the *M–N* domains for (a) piers (EPP-NTR model) and (b) spandrel (EPP-TR-CF and EPP-TR-TF models), with the sectional analysis and the MBA approach.

For the spandrel, the elastic–perfectly plastic stress–strain law and tensile resistant model (EPP-TR) is assumed. A compression governed model (EPP-TR-CF) with compressive strain ductility of $\mu_{\varepsilon c} = 1.2$ and $\mu_{\varepsilon c} = 3.5$ is adopted (assuming again $\varepsilon_{yc} = 1\%$). Furthermore, a tension governed model (EPP-TR-TF) with a tension strain ductility of $\mu_{\varepsilon t} = 50$ is considered (with $\varepsilon_{yt} = 0.04\%$ and $\varepsilon_{ut} = 2\%$), as suggested in Knox [55].

Similarly to the case of piers, the *M–N* domains for the spandrel expand in line with the increase of $\mu_{\varepsilon c}$ (from 1.2 to 3.5). The EPP-TR-CF and EPP-TR-TF models give the same results when $\mu_{\varepsilon c}$ is equal to 3.5 and $\mu_{\varepsilon t}$ is equal to 50, either using the traditional sectional analysis or the MBA approach. It is worth noting that the advantage of using the MBA procedure is to capture the step-by-step development of the neutral axis position in absence of compatibility conditions at section level, and thus be able to capture the full rocking motion and moment–rotation curve, instead of only the ultimate state strength.

Henceforward, the spandrel tensile behavior is considered in correspondence with the experimental results, in which the interlocking effect of bricks at the spandrel-joint interface region occurs. Furthermore, the EPP-TR-TF model is adopted for the flexural response of the spandrel, in which lower values for the rotation, flexural ductility and tensile strain ductility are conservatively assumed.

4.3 Subassembly level analysis: hierarchy of strength

The evaluation of the hierarchy of strength between the components of the subassembly (i.e., the piers and the spandrel) is based on the assessment of the individual capacities, by taking a common parameter as a reference, which is, in this case, the equivalent bending moment at the pier involved. The pier *M–N* interaction (or performance) domain is used to identify the sequence of failure mechanisms in each pier-spandrel subassembly. In this domain, the demand in terms of axial load variation, due to the horizontal force applied to the structure, is defined.

The capacity of the spandrel in terms of the equivalent pier bending moment is defined depending on the type of subassembly, and then considering a local (rotational) equilibrium between pier and spandrel. In the structure under study, both subassemblies are of type "external corner", and therefore are characterized by a "one-to-one" (no. of piers-to-no. of spandrels connecting into the joint) moment ratio.

A null value of the axial load acting on the spandrel has been assumed according to the specifications in the Italian code (NTC 2018 [25]). Although there is an axial compressive force on the spandrel that affects the strength envelope of the masonry, the latter normative recommends disregarding it to give a conservative estimate of the capacity. It is considered an acceptable approach, since low compression stress gradients are observed in spandrels due to the variation of the axial load on the piers, e.g. [8,9]. So, despite Equation (1) is used to estimate the equivalent tensile strength of the masonry (related to the interlocking effect, which is assumed to be constant) and the flexural capacity of the spandrel, the hypothesis of null axial load on the spandrel is considered. Therefore, the spandrel moment capacity is assumed to be constant within the *M–N* performance domain.

The *M–N* performance domain of the piers (it is the same for both piers), with the curves corresponding to the potential failure mechanisms of the piers and the spandrel, are shown in Figure 9a. The sequences of events in the right subassembly, subjected to a decrease of axial load ($-\Delta N$) (squares; numbered from 1 to 2), and in the left subassembly, subjected to an increase of axial load ($+\Delta N$) (triangles; numbered from 1 to 2) are illustrated in Figure 9b. In the right subassembly, the onset of failure is given by (i) diagonal cracking shear of the spandrel, followed by (ii) rocking of the pier. Instead, in the left subassembly, it is given by (i) diagonal cracking shear of the spandrel, followed by (ii) diagonal cracking of the pier.

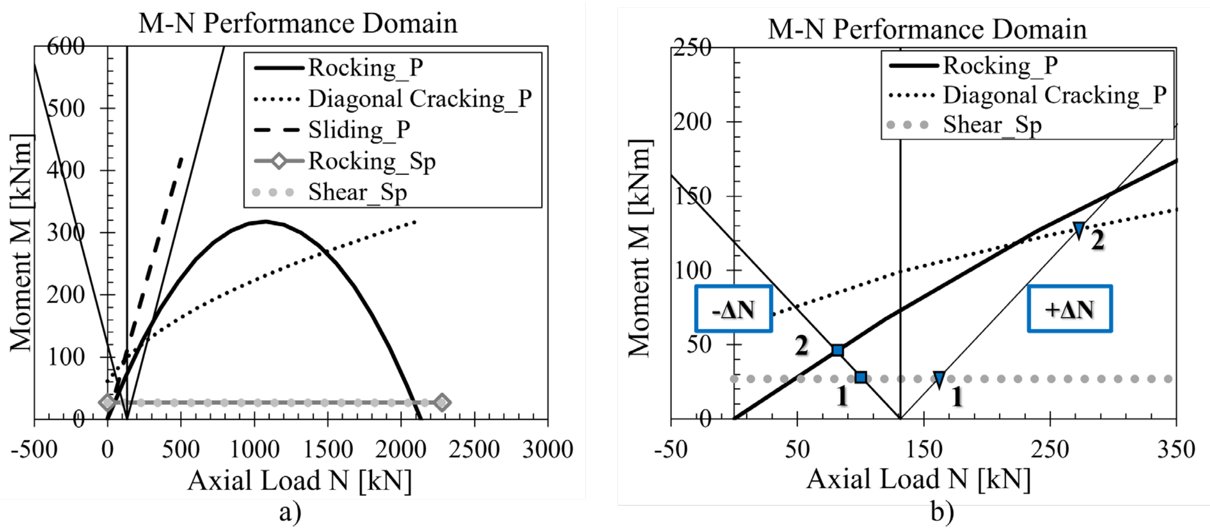

Figure 9. Frame analysis: (a) *M–N* performance domain; (b) zoom highlighting the sequence of failure events (■: right subassembly (–Δ*N*), ▼: left subassembly (+Δ*N*)).

4.4 Global level analysis: capacity curve

The global mechanism of the substructure, which is, in this case, a "mixed sideway" mechanism, can be defined based on the hierarchy of strength in each subassembly. The mechanism is characterized by the shear failure of the spandrel followed by the rocking of both piers, as also obtained from the experimental test and the numerical simulation.

The SLaMA method considers a bilinear elastic–perfectly plastic curve as a first approximation to the base shear force–displacement response of the structure. The elastic-limit and ultimate displacements of the bilinear curve are obtained according to the corresponding rotations of the critical structural components. Refinements to this curve are possible by evaluating the aforementioned OTM at intermediate stages (e.g., for different limit states). By calculating the OTM at different stages, starting from the limit elastic condition (identified as the rotation corresponding to the spandrel shear failure), a refined curve is obtained (see Figure 10a). Here, one may note that after the occurrence of shear damage in the spandrel, its relative contribution for the substructure's moment capacity decreases; thence, the effective height of the structure H_{eff} is supposed to increase. Note, however, that the change in H_{eff} is only reflected when using the refined SLAMA method since it is evaluated for different stages in the sequence of events. This parameter, together with the different values for the Overturning Moment (OTM) determines, according to Equation (9), the change in the initial slope of the curves in Fig. 10a.

To what concerns Figure 10b, it is evidenced that the refined curve is in better agreement with the experimental and numerical responses. The difference in terms of dissipated energy (i.e., the area under the curve) when comparing the standard and the refined curves with the experimental one is 10% and 8%, respectively. The predicted shear mechanism (brittle failure) of the spandrel occurs for a slightly lower displacement (marked with an "X" in the graphs). Finally, assuming that the structure is still capable of withstanding the lateral load, a global rocking mechanism is developed up to a displacement of 32 mm.

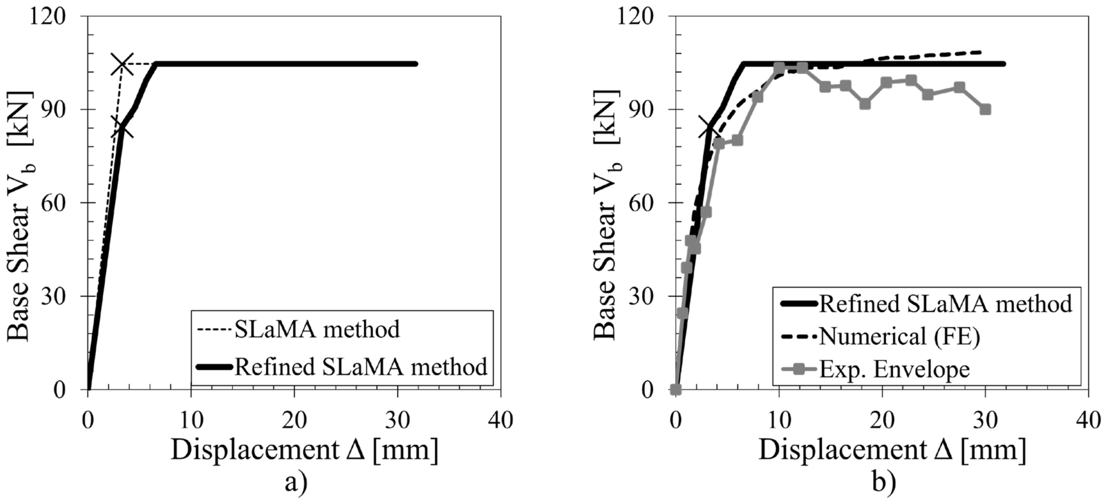

Figure 10. Global mechanism analysis: (a) analytical curves from the standard and refined SLaMA-URM procedures; (b) experimental, numerical, and analytical (refined) responses.

5. GEOMETRY INFLUENCE ON THE GLOBAL FAILURE MECHANICSM AND CAPACITY

The geometry of the structural components in URM structures plays an important role in the global seismic capacity. By varying the dimensions of piers and/or spandrels, the failure mechanism in each subassembly may change. To assess this influence, parametric analyses on the PS3 substructure were carried out and the *M–N* performance domains, together with the corresponding pushover curves, were obtained. The geometric configurations considered are listed in Table 4, where bold-marked values refer to variations in relation to the geometry of the PS3 substructure (in the first row, in italics). The effective length of the spandrel L_{sp} (clear span of the openings) and its height (or section depth) h_{sp}, as well as the length (or section depth) of the piers B_p and its height (clear, not effective) h_p were varied, individually, in the following ranges: L_{sp} = [1.24 - 2.50 m]; h_{sp} = [0.94 - 2.00 m]; B_p = [0.80 - 1.80 m]; h_p = [1.00 - 3.00 m]. Accordingly, the aspect ratios of the spandrel and piers vary in the range $\lambda_{sp} = L_{sp}/h_{sp}$ = [0.62 - 2.66] and $\lambda_p = h_p/B_p$ = [0.84 - 2.52], respectively.

It is worth noting that, in the following analyses, the PS3 specimen is considered as a benchmark and the shear failure of its spandrel corresponds to the ultimate state of the substructure. The analysis in this section is intended to investigate the influence of the substructure geometry on the results calculated according to the assumptions and formulation of the proposed SLaMA-URM procedure. It also allows to form an idea of possible limitations of the method for certain ranges of dimensions of the panels. Unlike the previous assumption in Section 4.4 of a global rocking mechanism of the substructure to allow extending its response (horizontal plateau) in displacement, here such a mechanism and the ductility branch are considered only when the spandrel fails by rocking, because the generalization of the previous assumption needs further evidence. This is evidenced in Table 4, where the determining failure mechanism for the pier-spandrel substructure is indicated.

Table 4. Description of the parametric analyses in relation to the PS3 substructure geometry (1st row in italics) and predicted failure mechanism. The varying geometric parameters are in bold.

h_p [m]	B_p [m]	λ_p [-]	L_{sp} [m]	h_{sp} [m]	λ_{sp} [-]	Failure mechanism
1.795	*1.19*	*1.51*	*1.24*	*0.94*	*1.32*	*SP Shear*
1.795	1.19	1.51	**1.40**	0.94	**1.49**	*SP Rocking*
1.795	1.19	1.51	**1.60**	0.94	**1.70**	*SP Rocking*
1.795	1.19	1.51	**1.80**	0.94	**1.91**	*SP Rocking*
1.795	1.19	1.51	**2.00**	0.94	**2.13**	*SP Rocking*
1.795	1.19	1.51	**2.20**	0.94	**2.34**	*SP Rocking*
1.795	1.19	1.51	**2.50**	0.94	**2.66**	*SP Rocking*
1.795	1.19	1.51	1.24	**1.20**	**1.03**	*SP Shear*
1.795	1.19	1.51	1.24	**1.50**	**0.83**	*SP Shear*
1.795	1.19	1.51	1.24	**2.00**	**0.62**	*SP Shear*
1.795	**0.80**	**2.24**	1.24	0.94	1.32	*SP Shear*
1.795	**1.00**	**1.80**	1.24	0.94	1.32	*SP Shear*
1.795	**1.40**	**1.28**	1.24	0.94	1.32	*SP Shear*
1.795	**1.60**	**1.12**	1.24	0.94	1.32	*SP Shear*
1.795	**1.80**	**1.00**	1.24	0.94	1.32	*SP Shear*
1.00	1.19	**0.84**	1.24	0.94	1.32	*SP Shear*
1.30	1.19	**1.09**	1.24	0.94	1.32	*SP Shear*
1.50	1.19	**1.26**	1.24	0.94	1.32	*SP Shear*
2.00	1.19	**1.68**	1.24	0.94	1.32	*SP Shear*
2.30	1.19	**1.93**	1.24	0.94	1.32	*SP Shear*
2.60	1.19	**2.18**	1.24	0.94	1.32	*SP Shear*
3.00	1.19	**2.52**	1.24	0.94	1.32	*SP Shear*

SP is for Spandrel.

From the performed analyses, it is highlighted that by increasing the length of the spandrel L_{sp} (for a given height, so increasing the aspect ratio), its failure mechanism changes from shear to flexural type (from λ_{sp} = 1.49) and, after this, although the base shear capacity is slightly reduced, the substructure show an increase in ductility μ (from 1.7 up to 2.3), see Figure 11a. Note that when the spandrel fails by shear, the lines in Figure 11 represent only the yield limit of the substructure. Contrarily, the spandrel capacity increases when its height h_{sp} is increased, and it continues to be governed by a shear failure without changing the original failure mechanism of the substructure (Figure 11b). In this case, there is a small increase of the base shear capacity of the substructure ranging between 6% to 12%. The influence of the spandrel length and depth is yet so pronounced as expected (up to 15% difference in base shear capacity), even if a significant change of ductility is observed when varying the spandrel length.

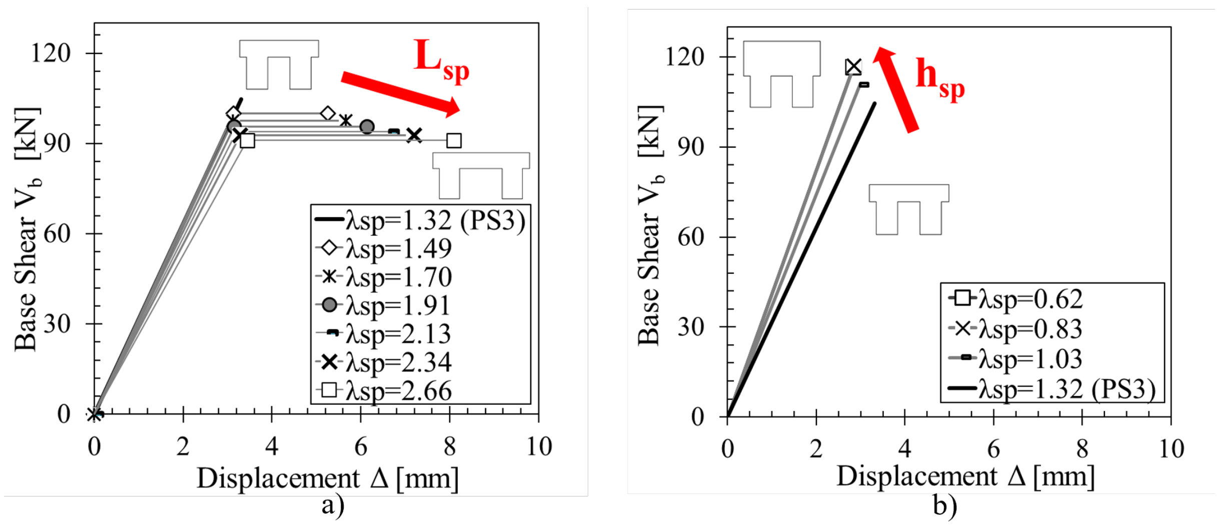

Figure 11. Capacity curves of the substructures when varying the (a) spandrel length L_{sp} and (b) spandrel height h_{sp}. Note: when the spandrel fails by shear, the lines represent only the yield limit.

Regarding the piers, an increase of the axial load ($+\Delta N$) leads to a rocking mechanism of the left pier for an aspect ratio λ_p larger than 1.26, while for lower values it presents a diagonal cracking failure. According to Figure 12a, the base shear capacity of the substructure increases for larger B_p lengths, within a –27% to +42% variation in relation to the PS3 substructure (black line in Figure 12a). In this case, the failure mechanism of the spandrel is not changed, i.e., it remains a shear failure. By varying the pier height h_p, the substructure has a significant change of stiffness and base shear strength, within –57% to +140% and –35% to +54% variation ranges, respectively, in relation to the PS3 substructure (black line in Figure 12b); the spandrel has a shear failure. At last, it is important to recall that the spandrel was always the "weakest link" and is then the first element to fail. Nonetheless, in other scenarios, the spandrel can have significantly higher strength, causing the piers to fail first, and therefore, the axial force redistribution may change. This possibility has not yet been explored in this work.

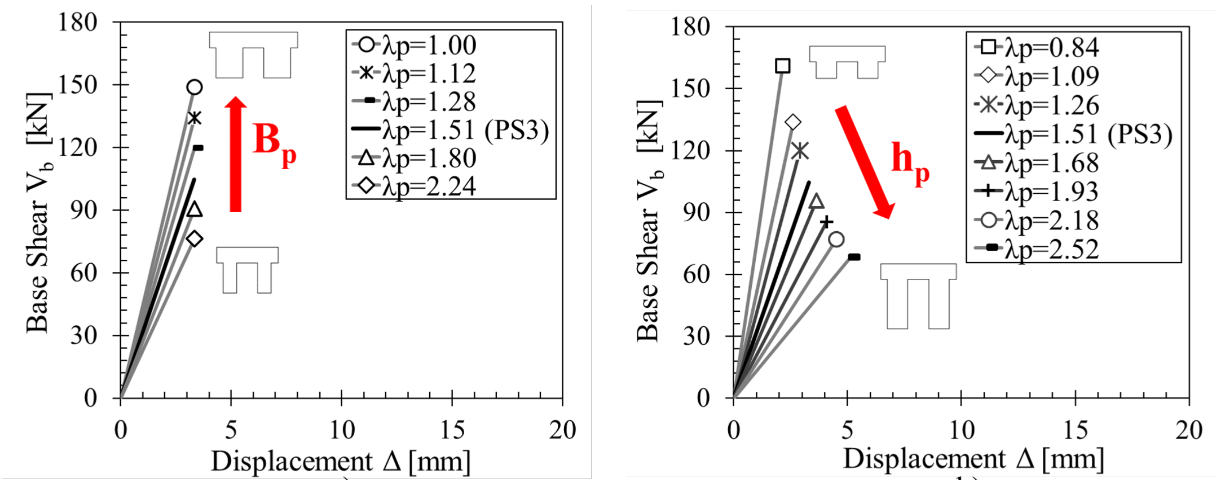

Figure 12. Capacity curves of the substructures when varying the (a) piers length B_p and (b) piers height h_p. Note: when the spandrel fails by shear, the lines represent only the yield limit.

6. ANALYTICAL-BASED STRENGTH OF URM PIER-SPANDREL JOINT

In the previous sections, the influence of the URM pier-spandrel joints on the global capacity of the structure was neglected since these components were assumed as rigid. Here, an analytical approach to derive the strength capacity of the pier-spandrel joints is considered with the aim to assess its effect on the pier M–N performance domain and hierarchy of strength of the subassembly. Four potential failure mechanisms of URM pier-spandrel joints are addressed: diagonal compression, toe crushing, sliding shear, and diagonal shear (tension).

An equivalent diagonal strut mechanism within the pier-spandrel joint is assumed, following the analogy with the failure mechanisms (and their hierarchy) of masonry infill walls within a RC frame [40]. According to this hypothesis, the diagonal strut resistance of the pier-spandrel joint is defined as the lowest strength amongst the aforementioned possible failure mechanisms, formulated by analogy with the corresponding failure modes in masonry infill walls. Details of such formulation are given in Appendix B.

The procedure is demonstrated with reference to the previously analyzed PS3 substructure. Firstly, the capacity of the pier-spandrel joints in terms of the equivalent bending moment of the pier needs to be calculated. To this aim, based on simplified equilibrium equations, the equivalent pier shear force and, subsequently, the pier equivalent moment, are obtained. The pier equivalent shear force V_p is defined from the lateral resistance of the equivalent strut V_{jh}, based on the geometry of the subassembly, as shown in Figure 13. The pier equivalent moment M_p is calculated multiplying V_p by the half pier height $h_p/2$ (assumed as the pier cantilever length). The expressions for V_p and M_p are formulated in Appendix A and the expression for V_{jh} is presented in Appendix B. Then, the hierarchy of strength between the pier, spandrel, and joint within the pier M–N performance domain is evaluated.

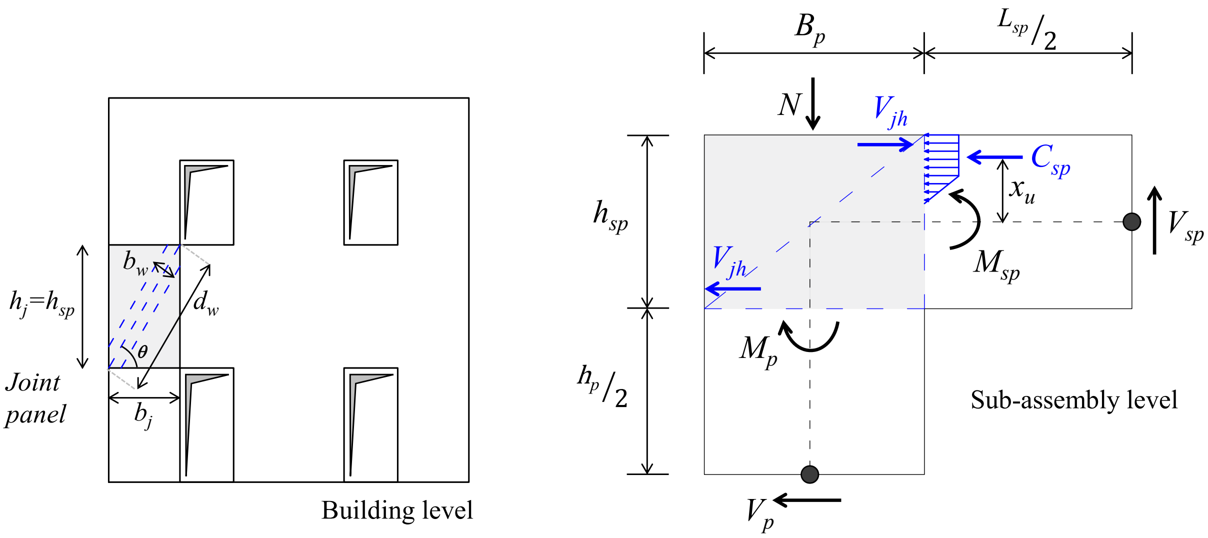

Figure 13. Schematization of the parameters to find the strength of a joint at a generic external subassembly (adapted from [20]).

For all cases investigated, the expected failure mechanism of the joints is diagonal cracking. The hierarchy of strength of the given substructures shows that when the spandrel height h_{sp} or the pier length B_p increase, the joint develops a higher capacity which can, by itself, be sufficient to prevent its failure when evaluating the sequence of events. On the contrary, the influence of the joint becomes important (i.e., its capacity decreases) when the pier height h_p or the spandrel length L_{sp} increases. To highlight this aspect, the capacity of the joints was considered in the pier M–N performance domains calculated for the performed parametric analyses. Some representative domains are presented in Figures 14 and 15, corresponding to subassemblies with varying the spandrel height h_{sp} and the spandrel length L_{sp}, respectively.

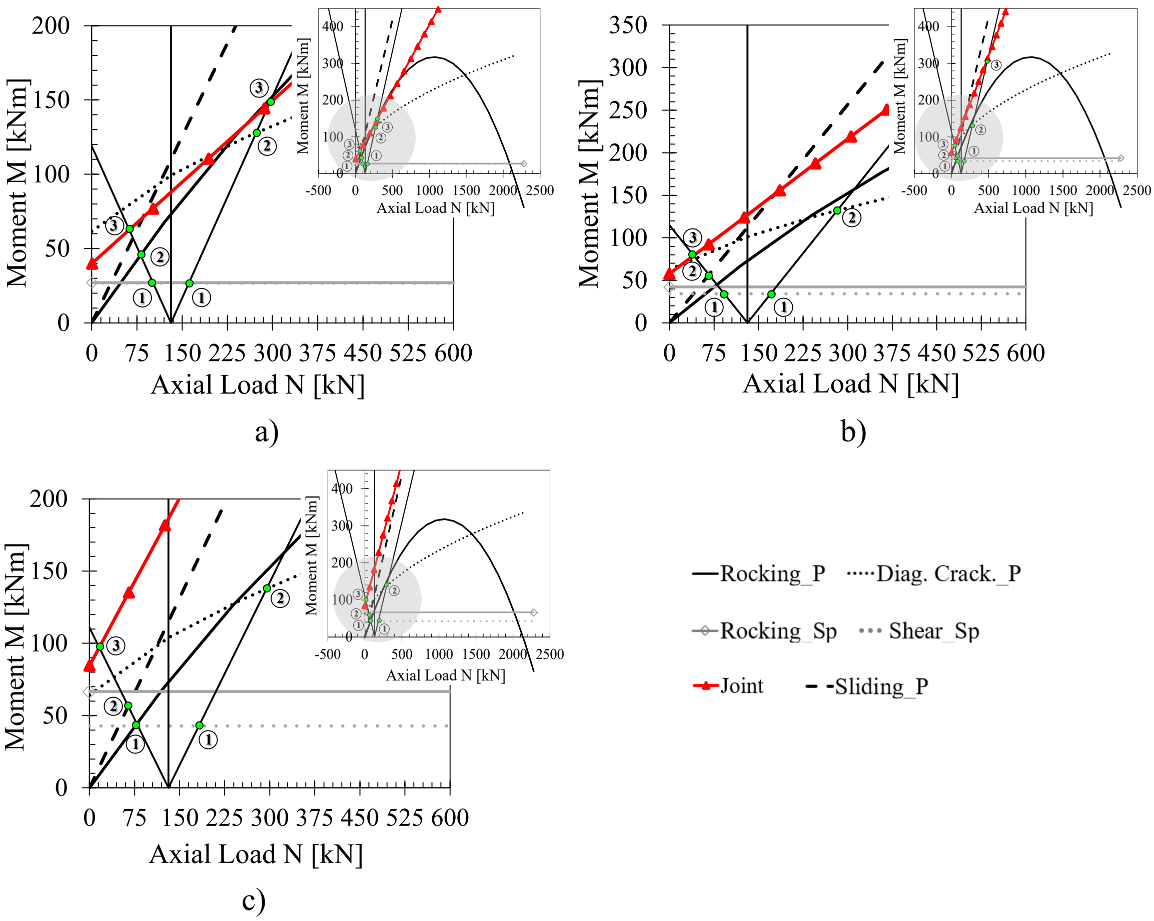

Figure 14. Pier *M–N* performance domains for subassemblies with an h_{sp} of (a) 0.94 m, (b) 1.20 m and (c) 1.50 m (circled numbers indicate the failure sequence events).

Both the spandrel height h_{sp} and the spandrel length L_{sp} influence the joint capacity consistently. For cases with low values of h_{sp} and/or high values of L_{sp} the capacity of the joint decreases and its influence on the hierarchy of strength could become significant. For example, when considering the case with L_{sp} equal to 2.50 m (Figure 15c) and the negative variation of axial load $-\Delta N$, the joint failure follows the rocking failure of the spandrel in the sequence of events. Hence, disregarding the finite actual capacity of the joint (as done when adopting the hypothesis of a rigid joint) could lead to incorrect and possibly unconservative predictions of both the local and global failure mechanisms and, in turn, to an inappropriate retrofit solution.

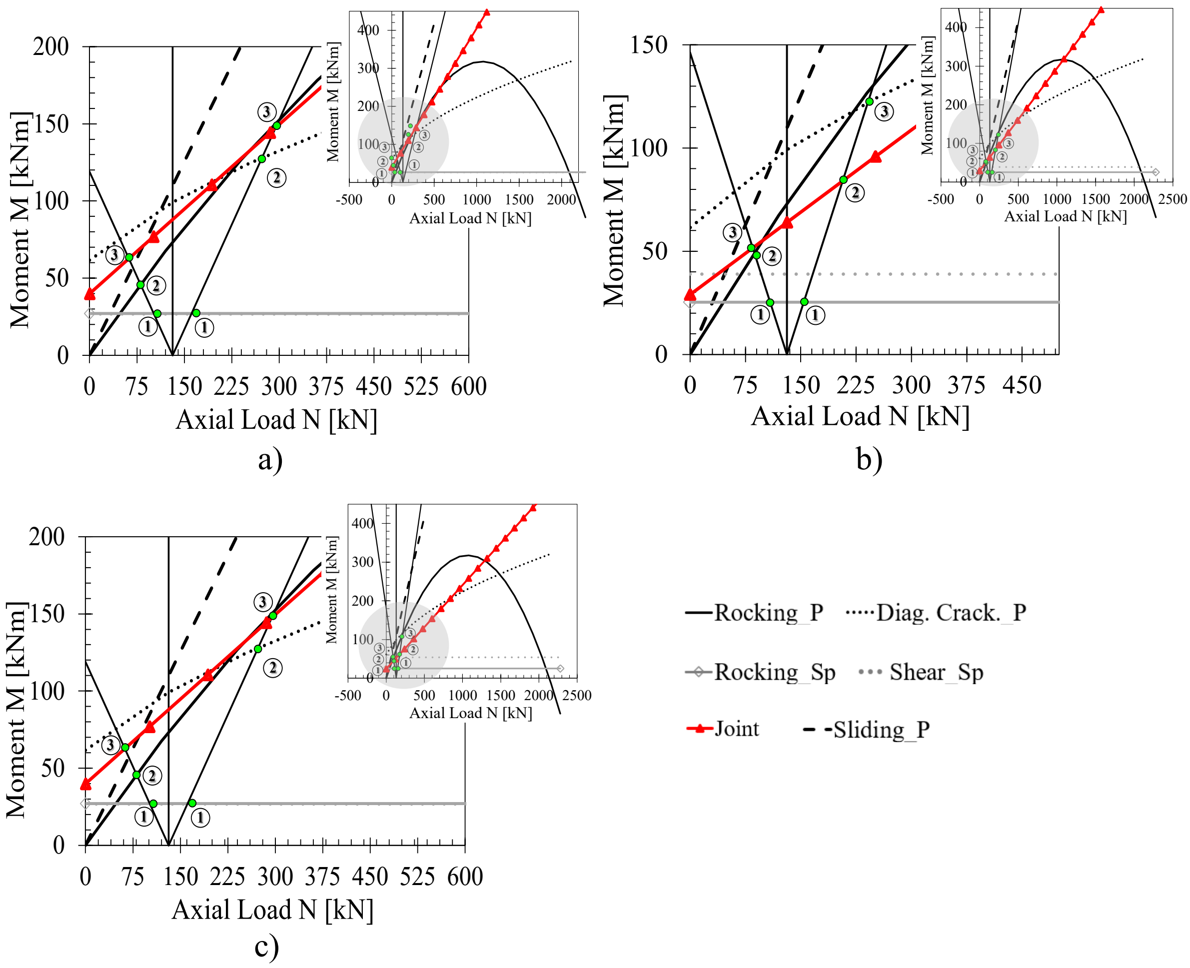

Figure 15. Pier *M–N* performance domains for subassemblies with an L_{sp} of (a) 1.24 m, (b) 1.80 m and (c) 2.50 m (circled numbers indicate the failure sequence events).

When increasing the spandrel length L_{sp}, the failure mechanism of the substructure is dominated by the flexural behavior of the spandrel. In this case, when the total length of the substructure increases, the variation of axial load ΔN due to the lateral load tends to decrease. For higher values of L_{sp}, the corresponding shear capacity of the spandrel increases. Regarding the analyzed variations of h_{sp}, B_p and h_p, the same failure mechanism observed for the PS3 substructure (i.e., starting with the shear failure of the spandrel) is identified.

The increase of h_{sp} leads to a higher variation of ΔN (due to the increased height of the substructure) and a slight increase of shear strength together with a large increase of flexural capacity of the spandrel. In this case, the joint capacity presents a significant increase. When the pier length B_p increases, a decrease of ΔN is observed (due to the increased length of the substructure); as expected, the flexural capacity of the piers increases, while the spandrel shear capacity decreases. Finally, for higher values of pier height h_p, the shear capacity of the piers increases and the joint capacity decreases.

7. CONCLUSIONS

In this paper, a novel extension of the SLaMA method to URM structures has been proposed. It aims to provide an estimation of the global seismic capacity of URM structures from the analysis at the member and subsystem levels. The experimental test of a one-story pier-spandrel substructure available in the literature was used as a benchmark to validate the SLaMA-URM method. A 2D macro-mechanical FE model was also developed to extend the results and complement the validation.

The proposed procedure defines the Moment–Axial load (*M–N*) performance domain of piers through a sectional analysis. Detailed constitutive laws for masonry, such as the strain-softening model, have been used instead of the compressive stress-block adopted in simplified methods. The Monolithic Beam Analogy approach was also adopted to define the moment–rotation curve of the deformable rocking piers. The results in terms of strength capacity are in very good agreement with those obtained from the traditional sectional analysis. The axial load variation on the piers, due to the coupling effect of the spandrel strip, has been shown to influence the hierarchy of strength and the sequence of failure mechanisms.

The obtained results with the SLAMA-URM method, in terms of crack patterns and capacity curves, are in relatively good agreement with the experimental and FE results, even when a bilinear curve approximation is used. A better agreement was achieved by implementing refinements to the proposed method, namely by evaluating the *OTM* in intermediate stages.

Parametric analyses of the structural geometry were also performed to get an idea of the limitations of the method for certain ranges of dimensions of the URM panels.

Although the pier-spandrel joint was initially considered as a rigid element, a new approach aiming at evaluating the strength capacity of the joint was proposed. A parametric analysis of the geometry of the pier-spandrel joint has shown that the traditional assumption of rigid joints is reasonable for large spandrel heights (typically greater than 1 m for common window and door openings). In other cases, such an assumption may lead to inaccurate and possibly unconservative results, so a clear indication of limiting geometric ratios is required.

The obtained results demonstrate that the SLaMA-URM method can be a valuable and practical approach to estimate the seismic capacity of URM buildings, as well as to support the design of retrofit solutions. Nonetheless, future studies should include the application and validation of the SLaMA-URM method to larger and more complex URM structures.

APPENDIX A. CALCULATION OF THE MAXIMUM PIER DEMAND V_P

A step-by-step demonstration to calculate the maximum shear demand for the pier V_p based on the rotational equilibrium of the pier-spandrel joint is given as follows:

1 The translational equilibrium of the internal forces can be written as:

$$V_{jh} = C_{sp} - V_p \tag{A.1}$$

where V_{jh} is the shear capacity of the joint panel, C_{sp} is the resultant of the compressive stresses on the spandrel edge, and V_p is the pier shear force. The shear capacity of the joint is computed according to the strategy given in Appendix B.

2 The rotational equilibrium is expressed as:

$$V_p \frac{h_p + h_{sp}}{2} = V_{sp} \frac{L_{sp} + B_p}{2} \tag{A.2}$$

3 From the rotational equilibrium the spandrel shear is defined in function of V_p, as:

$$V_{sp} = V_p \frac{h_p + h_{sp}}{L_{sp} + B_p} \tag{A.3}$$

4 The pier bending moment at the joint panel interface is given by $M'_p = V_p \frac{h_p}{2}$.

5 The spandrel moment at the joint panel interface is given by: $M'_{sp} = V_{sp} \frac{L_{sp}}{2} = C_{sp} x_u$, where x_u is the distance between the resulting compressive force (equivalent to a bilinear stress diagram) and the middle axis of the spandrel. Here, the neutral axis is computed considering only the compression stresses hence precluding the contribution of the tensile stresses. A no-tension assumption is therefore followed, which is fostered by its practical convenience and conservatism [56].

6 The resultant of the compression force on the masonry spandrel is derived from M'_{sp} and writing it as a function of V_p according to Equation (A.2), such as:

$$C_{sp} = \frac{M'_{sp}}{x_u} = \frac{V_{sp} \frac{L_{sp}}{2}}{x_u} = \frac{V_p}{2x_u} \frac{(h_p + h_{sp}) L_{sp}}{L_{sp} + B_p} \tag{A.4}$$

7 The shear capacity of the joint panel is, by considering Equation (A.4), expressed as a function of V_p:

$$V_{jh} = C_{sp} - V_p = V_p \left[\frac{(h_p + h_{sp}) L_{sp}}{2x_u (L_{sp} + B_p)} - 1 \right] \tag{A.5}$$

8 Therefore, the maximum shear demand for the pier can be written in terms of the shear joint capacity V_{jh}, i.e.:

$$V_p = \frac{V_{jh}}{\left[\frac{(h_p + h_{sp}) L_{sp}}{2x_u (L_{sp} + B_p)} - 1 \right]} \tag{A.6}$$

The equivalent pier moment M_p, associated with the joint shear capacity, is defined from multiplying V_p by the corresponding arm, so calculated as $M_p = V_p \frac{h_p + h_{sp}}{2}$.

APPENDIX B. CALCULATION OF THE SHEAR CAPACITY OF THE JOINT V_{JH}

The shear capacity of the joint V_{jh} is calculated by adapting the formulation given in [40] for masonry infill walls to the pier-spandrel joint panel (see Figure 13). In this scope, four potential failure modes are considered for the joint panel: (i) compression failure at the centre of the panel; (ii) compression failure at the corner edges; (iii) sliding shear failure; and (iv) diagonal tension failure. The strength of the equivalent strut is defined as the minimum value of the strength terms associated with the different mechanisms. Therefore, the corresponding horizontal capacity of the joint V_{jh} can be calculated by Equation (B.1).

$$V_{jh} = f_{strut} b_w t_j cos\theta \tag{B.1}$$

where b_w is the strut width, t_j is the joint thickness, θ is the strut angle, and f_{strut} is the strength of the equivalent strut given by $f_{strut} = \min(\sigma_{w,i})$, $i = 1,..,4$. The strength $\sigma_{w,i}$ is calculated for each failure mode. For the compression failure at the center of the joint panel, it is given as:

$$\sigma_{w,1} = \frac{1.16 f_{cm} tan\theta}{K_1 + K_2 \lambda h_j} \tag{B.2}$$

The strength for the compression failure at the corner edges of the joint panel is given as:

$$\sigma_{w,2} = \frac{1.12 f_{cm}\, sin\theta\, cos\theta}{K_1 (\lambda h_j)^{-0.12} + K_2 (\lambda h_j)^{0.88}} \tag{B.3}$$

The strength for the sliding shear failure of the joint panel is given as:

$$\sigma_{w,3} = \frac{(1.2 sin\theta + 0.45 cos\theta)(f_{v0} + \mu \sigma_v) + 0.3\sigma_v}{b_w / d_w} \tag{B.4}$$

The strength for the diagonal tension failure of the joint panel is given as:

$$\sigma_{w,4} = \frac{0.6 f_{ws} + 0.3\sigma_v}{b_w / d_w} \tag{B.5}$$

where f_{v0} is the masonry shear strength in absence of axial load; μ is the masonry friction coefficient (assumed as $\mu = 0.7$); σ_v is the vertical compressive stress on the joint panel due to the gravity load; b_w and d_w are the in-plane dimensions of the equivalent strut (see Figure 13);

h_j is the height of the joint panel (see Figure 13); f_{ws} is the shear strength of the diagonal equivalent strut, assumed as $f_{ws} = f_{v0}$; λ is found as given in Equation (B.6) when considering that the masonry has an elastic isotropic behavior; and K1 and K2 are, as proposed in [40], determined as a function of the resulting product λh_j as described in Equation (B.7).

$$\lambda = \sqrt[4]{\frac{12sen(2\theta)}{4b_j^3 h_j}} \tag{B.6}$$

$$\begin{cases} K1 = 1.3\,, K2 = -0.178 & if \quad \lambda h_J \leq 3.14 \\ K1 = 0.707\,, K2 = 0.01 & if \quad 3.14 < \lambda h_J < 7.85 \\ K1 = 0.47\,, K2 = 0.04 & if \quad \lambda h_J \geq 7.85 \end{cases} \tag{B.7}$$

DATA AVAILABILITY STATEMENT

The data that support the findings of this study will be made available from the corresponding author upon reasonable request.

ACKNOWLEDGEMENTS

The financial support to the first author by the Joint Research Project Program of University of Rome La Sapienza (DR 2289), in the form of traveling and living allowances during the stay at University of Minho, and by the ReLUIS Project WP7, funded by the Italian Civil Protection Department, in the form of a research scholarship, *is greatly acknowledged.*

REFERENCES

[1] P.B. Lourenço, L.C. Silva, Computational applications in masonry structures: from the meso-scale to the super-large/super-complex, Int. J. Multiscale Comput. Eng. 18 (2020) 1–30. https://doi.org/10.1615/IntJMultCompEng.2020030889.

[2] P. Roca, M. Cervera, G. Gariup, L. Pela', Structural Analysis of Masonry Historical Constructions. Classical and Advanced Approaches, Arch. Comput. Methods Eng. 17 (2010) 299–325. https://doi.org/10.1007/s11831-010-9046-1.

[3] S. Sharma, L.C. Silva, F. Graziotti, G. Magenes, G. Milani, Modelling the experimental seismic out-of-plane two-way bending response of unreinforced periodic masonry panels

using a non-linear discrete homogenized strategy, Eng. Struct. 242 (2021). https://doi.org/10.1016/j.engstruct.2021.112524.

[4] E. Bertolesi, L.C. Silva, G. Milani, Validation of a two-step simplified compatible homogenisation approach extended to out-plane loaded masonries, Int. J. Mason. Res. Innov. 4 (2019) 265. https://doi.org/10.1504/IJMRI.2019.10019407.

[5] M.F. Funari, L.C. Silva, N. Savalle, P.B. Lourenço, A concurrent micro/macro FE-model optimized with a limit analysis tool for the assessment of dry-joint masonry structures, Int. J. Multiscale Comput. Eng. 20 (2022) 65–85. https://doi.org/10.1615/IntJMultCompEng.2021040212.

[6] G. de Felice, S. De Santis, P.B. Lourenço, N. Mendes, Methods and Challenges for the Seismic Assessment of Historic Masonry Structures, Int. J. Archit. Herit. 11 (2017) 143–160. https://doi.org/10.1080/15583058.2016.1238976.

[7] P.B. Lourenço, N. Mendes, L.F. Ramos, D. V. Oliveira, Analysis of Masonry Structures Without Box Behavior, Int. J. Archit. Herit. 5 (2011) 369–382. https://doi.org/10.1080/15583058.2010.528824.

[8] R. Marques, P.B. Lourenço, Possibilities and comparison of structural component models for the seismic assessment of modern unreinforced masonry buildings, Comput. Struct. 89 (2011) 2079–2091. https://doi.org/10.1016/J.COMPSTRUC.2011.05.021.

[9] R. Marques, P.B. Lourenço, Unreinforced and confined masonry buildings in seismic regions: Validation of macro-element models and cost analysis, Eng. Struct. 64 (2014) 52–67. https://doi.org/https://doi.org/10.1016/j.engstruct.2014.01.014.

[10] M.F. Funari, L.C. Silva, E. Mousavian, P.B. Lourenço, Real-time Structural Stability of Domes through Limit Analysis: Application to St. Peter's Dome, Int. J. Archit. Herit. (2021) 1–23. https://doi.org/10.1080/15583058.2021.1992539.

[11] M. Valente, G. Milani, Seismic assessment of historical masonry towers by means of

simplified approaches and standard FEM, Constr. Build. Mater. 108 (2016) 74–104. https://doi.org/10.1016/J.CONBUILDMAT.2016.01.025.

[12] F. Clementi, V. Gazzani, M. Poiani, S. Lenci, Assessment of seismic behaviour of heritage masonry buildings using numerical modelling, J. Build. Eng. 8 (2016) 29–47. https://doi.org/https://doi.org/10.1016/j.jobe.2016.09.005.

[13] A. Formisano, G. Vaiano, F. Fabbrocino, G. Milani, Seismic vulnerability of Italian masonry churches: The case of the Nativity of Blessed Virgin Mary in Stellata of Bondeno, J. Build. Eng. 20 (2018) 179–200. https://doi.org/https://doi.org/10.1016/j.jobe.2018.07.017.

[14] M. Nunes, R. Bento, M. Lopes, In-plane stiffening and strengthening of timber floors for the improvement of seismic behaviour of URM buildings, Int. J. Mason. Res. Innov. 5 (2020) 85–120. https://doi.org/https://doi.org/10.1504/IJMRI.2020.104847.

[15] F. Vadalà, V. Cusmano, M.F. Funari, I. Caliò, P.B. Lourenço, On the use of a mesoscale masonry pattern representation in discrete macro-element approach, J. Build. Eng. 50 (2022) 104182. https://doi.org/https://doi.org/10.1016/j.jobe.2022.104182.

[16] M. Dolce, Schematizzazione e modellazione degli edifici in muratura soggetti ad azioni sismiche, L'industria Delle Costr. 242 (1991) 44–57.

[17] NZSEE, The Seismic Assessment of Existing Buildings: Part C5, Concrete Buildings, Technical Guidelines for Engineering Assessments, Wellington, New Zealand, 2017. http://www.eq-assess.org.nz/.

[18] Netherlands Standardization Institute (NEN), Assessment of Structural Safety of Buildings in Case of Erection, Reconstruction, and Disapproval—Induced Earthquakes—Basis of Design, Actions and Resistances, NPR 9998. (In Dutch), Delft, The Netherlands, 2018.

[19] R. Gentile, C. del Vecchio, S. Pampanin, D. Raffaele, G. Uva, Refinement and

Validation of the Simple Lateral Mechanism Analysis (SLaMA) Procedure for RC Frames, J. Earthq. Eng. 25 (2021) 1227–1255. https://doi.org/10.1080/13632469.2018.1560377.

[20] R. Gentile, S. Pampanin, D. Raffaele, G. Uva, Analytical seismic assessment of RC dual wall/frame systems using SLaMA: Proposal and validation, Eng. Struct. 188 (2019) 493–505. https://doi.org/https://doi.org/10.1016/j.engstruct.2019.03.029.

[21] M.J. Fox, B.A. Westeneng, C.A. Muir, A. Baird, W.Y. Kam, P.L. Beazley, R.. Jury, R.D. Sharpe, Simple lateral mechanism analysis (SLaMA) for the seismic assessment of unreinforced masonry structures, in: 17th World Conf. Earthq. Eng., Sendai, Japan, 2020: pp. 1–11.

[22] P. Stefano, B. Davide, P. Alberto, Performance-Based Seismic Retrofit Strategy for Existing Reinforced Concrete Frame Systems Using Fiber-Reinforced Polymer Composites, J. Compos. Constr. 11 (2007) 211–226. https://doi.org/10.1061/(ASCE)1090-0268(2007)11:2(211).

[23] F. Graziotti, U. Tomassetti, S. Sharma, L. Grottoli, G. Magenes, Experimental response of URM single leaf and cavity walls in out-of-plane two-way bending generated by seismic excitation, Constr. Build. Mater. 195 (2019) 650–670. https://doi.org/10.1016/j.conbuildmat.2018.10.076.

[24] G. Guerrini, I. Senaldi, F. Graziotti, G. Magenes, K. Beyer, A. Penna, Shake-Table Test of a Strengthened Stone Masonry Building Aggregate with Flexible Diaphragms, Int. J. Archit. Herit. 13 (2019) 1078–1097. https://doi.org/10.1080/15583058.2019.1635661.

[25] NTC, Aggiornamento Delle «Norme Tecniche Per Le Costruzioni - Ministerial Decree 17/01/2018, Gazzetta Ufficle dello Stato italiano, Rome, Italy, 2018.

[26] NZSEE, The Seismic Assessment of Existing Buildings: Part C8, Unreinforced Masonry Buildings, Technical Guidelines for Engineering Assessments, Wellington, New

Zealand, 2017.

[27] V. Turnšek, F. Čačovič, Some experimental results on the strength of brick masonry walls, in: Proc. 2nd Int. Brick Mason. Conf., Stoke-on-Trent: British Ceramic Research Association, 1971: pp. 149–156.

[28] W. Mann, H. Muller, Failure of shear-stressed masonry: an enlarged theory, tests and application to shear walls, in: Proceeding Br. Ceram. Soc., Stoke-on-Trent: British Ceramic Society, 1982: pp. 223–235.

[29] K. Beyer, A. Dazio, Quasi-static cyclic tests on masonry spandrels, Earthq. Spectra. 28 (2012) 907–929. https://doi.org/10.1193/1.4000063.

[30] F. Parisi, N. Augenti, A. Prota, Implications of the spandrel type on the lateral behavior of unreinforced masonry walls, Earthq. Eng. Struct. Dyn. 43 (2014) 1867–1887. https://doi.org/https://doi.org/10.1002/eqe.2441.

[31] C.L. Knox, D. Dizhur, J.M. Ingham, Experimental Cyclic Testing of URM Pier-Spandrel Substructures, J. Struct. Eng. 143 (2017) 04016177. https://doi.org/10.1061/(asce)st.1943-541x.0001650.

[32] EN1998-3:2005, Eurocode 8:2005. Design of structures for earthquake resistance - Part 3: Assessment and retrofitting of buildings, Brussels, Belgium, 2005.

[33] FEMA 306, Evaluation of earthquake damaged concrete and masonry wall buildings. Basic Procedures Manual, Washington, DC, USA, 1998.

[34] S. Cattari, S. Lagomarsino, A strength criterion for the flexural behavior of spandrels in un-reinforced masonry walls, in: International Association for Earthquake Engineering (Ed.), Proceeding 14th World Conf. Earthq. Eng., Beijing, China, 2008.

[35] A. Dazio, The effect of the boundary conditions on the out-of-plane behaviour of unreinforced masonry walls, in: Proc. 14th World Conf. Earthq. Eng. Oct. 12-17, 2008, Beijing China Innov. Pract. Saf., Chinese Association of Earthquake Engineering, 2008.

[36] C. Morandini, D. Malomo, A. Penna, Equivalent frame discretisation for URM façades with irregular opening layouts, Bull. Earthq. Eng. 20 (2022) 2589–2618. https://doi.org/10.1007/s10518-022-01315-0.

[37] A. Aşıkoğlu, G. Vasconcelos, P.B. Lourenço, B. Pantò, Pushover analysis of unreinforced irregular masonry buildings: Lessons from different modeling approaches, Eng. Struct. 218 (2020). https://doi.org/10.1016/j.engstruct.2020.110830.

[38] F. Parisse, S. Cattari, R. Marques, P.B. Lourenço, G. Magenes, K. Beyer, B. Calderoni, G. Camata, E.A. Cordasco, M.A. Erberik, C. İçel, M. Karakaya, D. Malomo, C.F. Manzini, C. Marano, F. Messali, G. Occhipinti, B. Pantò, Saygılı, M. Sousamli, Benchmarking the seismic assessment of unreinforced masonry buildings from a blind prediction test, Structures. 31 (2021) 982–1005. https://doi.org/10.1016/j.istruc.2021.01.096.

[39] E. Quagliarini, G. Maracchini, F. Clementi, Uses and limits of the Equivalent Frame Model on existing unreinforced masonry buildings for assessing their seismic risk: A review, J. Build. Eng. 10 (2017) 166–182. https://doi.org/10.1016/j.jobe.2017.03.004.

[40] S.H. Bertoldi, L.D. Decanini, C. Gavarini, Telai tamponati soggetti ad azioni sismiche, un modello semplificato: confronto sperimentale e numerico, in: Atti Del 6º Convegno ANIDIS, Associazione Nazionale Italiana di Ingegneria Sismica, (in Italian), Perugia, 1993: pp. 815–824.

[41] S. Lagomarsino, A. Penna, A. Galasco, S. Cattari, TREMURI program: An equivalent frame model for the nonlinear seismic analysis of masonry buildings, Eng. Struct. 56 (2013) 1787–1799. https://doi.org/10.1016/j.engstruct.2013.08.002.

[42] S. Pampanin, M.J. Nigel Priestley, S. Sritharan, Analytical modelling of the seismic behaviour of precast concrete frames designed with ductile connections, J. Earthq. Eng. 5 (2001) 329–368. https://doi.org/10.1080/13632460109350397.

[43] F. Graziotti, G. Magenes, A. Penna, Experimental cyclic behaviour of stone masonry spandrels, in: 15th World Conf. Earthq. Eng., Lisbon, Portugal, 2012. https://www.iitk.ac.in/nicee/wcee/article/WCEE2012_3261.pdf.

[44] G. Magenes, G. Kingsley, G.M. Calvi, Seismic Testing of a Full-Scale, Two-Story Masonry Building: Test Procedure and Measured Experimental Response, Pavia, 1995.

[45] G. Magenes, G.M. Calvi, In-plane seismic response of brick masonry walls, Earthq. Eng. Struct. Dyn. 26 (1997) 1091–1112. https://doi.org/10.1002/(SICI)1096-9845(199711)26:11<1091::AID-EQE693>3.0.CO;2-6.

[46] U. Akguzel, S. Pampanin, Effects of Variation of Axial Load and Bidirectional Loading on Seismic Performance of GFRP Retrofitted Reinforced Concrete Exterior Beam-Column Joints, J. Compos. Constr. 14 (2010) 94–104. https://doi.org/10.1061/(asce)1090-0268(2010)14:1(94).

[47] M.J.N. Priestley, G.M. Calvi, Kowalsky, Displacement-Based Seismic Design of Structures, Pavia, Italia, 2007.

[48] T. Celano, L.U. Argiento, F. Ceroni, C. Casapulla, Literature Review of the In-Plane Behavior of Masonry Walls: Theoretical vs. Experimental Results, Mater. . 14 (2021). https://doi.org/10.3390/ma14113063.

[49] N. Mendes, P.B. Lourenço, Sensitivity analysis of the seismic performance of existing masonry buildings, Eng. Struct. 80 (2014) 137–146. https://doi.org/10.1016/j.engstruct.2014.09.005.

[50] S. Saloustros, L. Pelà, M. Cervera, P. Roca, An Enhanced Finite Element Macro-Model for the Realistic Simulation of Localized Cracks in Masonry Structures: A Large-Scale Application, Int. J. Archit. Herit. 12 (2018) 432–447. https://doi.org/10.1080/15583058.2017.1323245.

[51] DIANA, 2019, DIsplacement ANAlyzer finite element software package, version 10,

DIANA FEA, Delft, https://dianafea.com, n.d.

[52] P.B. Lourenço, Recent advances in masonry modelling: micromodelling and homogenisation, in: Multiscale Model. Solid Mech., Imperial College Press, 2009: pp. 251–294. https://doi.org/10.1142/9781848163089_0006.

[53] B.V. Wilding, K.M. Dolatshahi, K. Beyer, Influence of load history on the force-displacement response of in-plane loaded unreinforced masonry walls, Eng. Struct. 152 (2017) 671–682. https://doi.org/https://doi.org/10.1016/j.engstruct.2017.09.038.

[54] R. Lumantarna, D.T. Biggs, J.M. Ingham, Uniaxial Compressive Strength and Stiffness of Field-Extracted and Laboratory-Constructed Masonry Prisms, J. Mater. Civ. Eng. 26 (2014) 567–575. https://doi.org/10.1061/(ASCE)MT.1943-5533.0000731.

[55] C. Knox, Assessment of perforated unreinforceds masonry walls responding in-plane, PhD thesis, 2012. https://hdl.handle.net/2292/19422.

[56] M. Angelillo, P.B. Lourenço, G. Milani, Masonry behaviour and modelling, in: M. Angelillo (Ed.), CISM Int. Cent. Mech. Sci. Courses Lect., 2014: pp. 1–26. https://doi.org/10.1007/978-3-7091-1774-3_1.